JOURNAL OF AIRCRAFT
Vol. 47, No. 2, March–April 2010

Numerical Study of Flow Past Circular Cylinder Using Hybrid Turbulence Formulations

Alaa Elmiligui* and Khaled S. Abdol-Hamid†
NASA Langley Research Center, Hampton, Virginia 23681
Steven J. Massey‡
Eagle Aeronautics, Inc., Hampton, Virginia 23669
and
S. Paul Pao§
NASA Langley Research Center, Hampton, Virginia 23681

DOI: 10.2514/1.18765

Two multiscale-type turbulence models are implemented in the PAB3D solver. The models are based on modifying Reynolds-averaged Navier–Stokes equations. The first scheme is a hybrid Reynolds-averaged Navier–Stokes and large eddy simulation model using the two-equation $k\varepsilon$ model with a Reynolds-averaged Navier–Stokes and large eddy simulation transition function dependent on grid spacing and the computed turbulence length scale. The second scheme is a modified version of the partially averaged Navier–Stokes model, where the unresolved kinetic energy parameter f_k is allowed to vary as a function of grid spacing and the turbulence length scale. Solutions from these models are compared to Reynolds-averaged Navier–Stokes results and experimental data for a stationary and rotating cylinder. The parameter f_k varies between zero and one and has the characteristic to be equal to one in the viscous sublayer, and when the Reynolds-averaged Navier–Stokes turbulent viscosity becomes smaller than the large eddy simulation viscosity. The formulation, usage methodology, and validation example are presented to demonstrate the enhancement of PAB3D's time-accurate and turbulence modeling capabilities. The models are compared to Reynolds-averaged Navier–Stokes results and experimental data for turbulent separated flows and laminar separated flows around stationary and rotating cylinders. For a stationary cylinder, the turbulent separated case is accurately simulated using the general two-equation $k\varepsilon$ turbulence model (eddy-viscosity model). PAB3D accurately predicts the drag coefficient C_D, lift coefficient C_L, and the Strouhal number St. The laminar separated case was a challenge for the Reynolds-averaged Navier–Stokes computation with an eddy-viscosity turbulence model. The Reynolds-averaged Navier–Stokes with large eddy simulation and partially averaged Navier–Stokes performed well and showed marked improvements over the Reynolds-averaged Navier–Stokes solution. The modified partially averaged Navier–Stokes model was the most accurate. For the rotating cylinder, the spin ratio varied from zero to one, and the partially averaged Navier–Stokes results were in good agreement with published experimental data. Reynolds-averaged Navier–Stokes with large eddy simulation and partially averaged Navier–Stokes capture both temporal and spatial fluctuations and produce large-scale structures that do not occur in the Reynolds-averaged Navier–Stokes simulation. The current results show promise for the capability of partially averaged Navier–Stokes in simulating unsteady and complex flow phenomena.

I. Introduction

THE limited capability of the Reynolds-averaged Navier–Stokes (RANS) approach, combined with eddy-viscosity turbulence models to simulate unsteady and complex flows, has been well known for some time. The RANS assumes that most of the energy is modeled through turbulence transport equations and is resolved in the grid. RANS also overpredicts the eddy viscosity, which results in excessive damping of unsteady motion. Consequently, the eddy viscosity of the unresolved scales attains unphysical large values suppressing most temporal and spatial fluctuations in the resolved flowfield. One of the approaches to overcome this problem is to provide the required mechanism to resolve the largest scales of motion. Among several methods, the detached eddy simulations (DES) [1], hybrid large eddy simulation (LES) [2,3], limited numerical scheme (LNS) [4], and partially averaged Navier–Stokes (PANS) [5] are capable of providing the needed mechanism to satisfy this requirement. One of the major deficiencies associated with the heretofore published use of hybrid schemes is that there is no clear identification of the different flow regions. These regions need to be clearly defined as RANS regions and hybrid regions to achieve complete simulation, independent of grid resolution. Several researchers observed that in most cases, using hybrid methods, the use of fine grid might result in incorrect simulations. Abdol-Hamid and Girimaji [6] explored a new approach to improve the accuracy and robustness of creating a simulation of an unsteady flowfield based on the work by [6]. They accomplished this through the development and implementation of a novel two-stage procedure to efficiently estimate the level of scale resolution possible for a given flow on a given grid for PANS and other hybrid models.

PAB3D is a structured, multiblock, parallel, implicit, finite volume solver of the three-dimensional RANS equations, and advanced turbulence models are available in the code. PAB3D is widely used for internal and external flow applications by NASA and by the U.S. aerospace industry. Investigations in the area of unsteady flow control for propulsion applications have led to an increased interest in upgrading PAB3D's [7,8] time-accurate capabilities. The current

Presented as Paper 4959 at the 22nd Applied Aerodynamics Conference and Exhibit, Providence, RI, 16–19 August 2004; received 11 July 2005; revision received 9 November 2005; accepted for publication 23 November 2005.

*Aerospace Research Engineer, Configuration Aerodynamics Branch, Mail Stop 499. Member AIAA.
†Senior Research Scientist, Configuration Aerodynamics Branch, Mail Stop 499. Associate Fellow AIAA.
‡Senior Research Scientist, 13 West Mercury Boulevard. Member AIAA.
§Senior Research Scientist, Configuration Aerodynamics Branch, Mail Stop 499. Senior Member AIAA.

version of the PAB3D code has a second-order time-accuracy algorithm scheme by employing either physical time with subiteration or dual time subiteration [8].

In an attempt to increase the flow physics fidelity and the accuracy of PAB3D code, hybrid turbulence model RANS/LES [2,3] has been added. An alternate new feature to PAB3D is the addition of the PANS method, which was suggested by Girimaji et al. [5]. The PANS model was developed to overcome the grid dependency associated with the customary implementation of the hybrid RANS/LES method. The addition of improved algorithms for second-order time accuracy, subiteration schemes, hybrid turbulence modeling, and moving boundary conditions provides key modernizing enhancements to the code. The primary objective of this paper is to assess the performance of these newly implemented approaches in a production computational fluid dynamics (CFD) code.

The organization of the paper is as follows: The governing equations of the RANS, RANS/LES, and PANS formulation will be presented and discussed in detail. Computational results from RANS, RANS/LES, and PANS for a flow past a stationary and a rotating cylinder will be presented and compared to experimental data. Flow around a cylinder is considered as the test case for the hybrid turbulence model [9–13], because it is a basic engineering problem and is inherently unsteady.

II. Approach

The governing equations of the RANS formulation include the conservation equations for mass, momentum, energy, and the equation of state. In the present study, the perfect gas law is chosen to represent the air properties, and the eddy-viscosity concept is used to model the Reynolds stresses. The mass, momentum, and energy conservation equations of the RANS equations can be written in a conservative form as follows:

$$\frac{\partial \rho}{\partial t} + \frac{\partial \rho u_i}{\partial x_i} = 0$$

$$\frac{\partial \rho u_i}{\partial t} + \frac{\partial (\rho u_i u_j + p\delta_{ij})}{\partial x_j} = \frac{\partial (\tau_{ij} - \rho \overline{u_i u_j})}{\partial x_j} \tag{1}$$

$$\frac{\partial \rho e_0}{\partial t} + \frac{\partial (\rho e_0 u_i + p u_i)}{\partial x_i} = \frac{\partial (\tau_{ij} u_j - \rho \overline{u_i u_j u_j})}{\partial x_i} - \frac{\partial (q_i + C_P \rho \overline{u_i \theta})}{\partial x_i} + \frac{\partial}{\partial x_i}\left[\rho\left(\nu_l + \frac{\nu_t}{\bar{\sigma}_k}\right)\frac{\partial k}{\partial x_i}\right]$$

To close the RANS equations, the two-equation $k\varepsilon$ turbulence model is used:

$$\frac{\partial \rho k}{\partial t} + \frac{\partial \rho u_j k}{\partial x_j} = -\rho \overline{u_j u_i}\frac{\partial u_i}{\partial x_j} + \frac{\partial}{\partial x_j}\left[\rho\left(\nu_l + \frac{c_\mu k^2}{\bar{\sigma}_k \varepsilon}\right)\frac{\partial k}{\partial x_j}\right] - \rho\varepsilon \tag{2}$$

$$\frac{\partial \rho \varepsilon}{\partial t} + \frac{\partial \rho u_j \varepsilon}{\partial x_j} = -C_{\varepsilon 1}\rho \overline{u_j u_i}\frac{\partial u_i}{\partial x_j}\frac{\varepsilon}{k} + \frac{\partial}{\partial x_j}\left[\rho\left(\nu_l + \frac{c_\mu k^2}{\bar{\sigma}_\varepsilon \varepsilon}\right)\frac{\partial \varepsilon}{\partial x_j}\right] - f_2 \tilde{C}_{\varepsilon 2}\rho\frac{\varepsilon}{k}\left[\varepsilon - \nu_l\left(\frac{\partial \sqrt{k}}{\partial x_j}\right)^2\right] \tag{3}$$

$$C_\mu = 0.09, \qquad C_{\varepsilon 1} = 1.44, \quad \text{and} \quad \overline{C_{\varepsilon 2}} = C_{\varepsilon 2} = 1.92$$

$$f_\mu = \exp\left[\frac{-3.41}{(1 + \frac{R_T}{50})^2}\right], \qquad R_T = \frac{k^2}{\nu_t \varepsilon}$$

$$f_2 = 1.0 - 0.3\exp(-R_T^2)$$

The boundary conditions for ε and k at the wall are

$$\varepsilon_{\text{wall}} = \nu_l\left(\frac{\partial \sqrt{k}}{\partial n}\right)^2$$

and $k_{\text{wall}} = 0$.

In the present paper, we use the simple eddy diffusivity (SED) approach, which is based on the Boussinesq viscosity model. This approach is used to model all the scalar diffusion terms appearing in the RANS and standard $k\varepsilon$ equations. For the heat flux term, the SED is written as follows:

$$\rho \overline{u_i \theta} = -\frac{\rho \upsilon_t}{\sigma_\tau}\frac{\partial T}{\partial x_i} \quad \text{and} \quad \sigma_\tau = 0.9$$

The turbulent stress components are formulated as

$$\rho \overline{u_j u_i} = 2\rho \upsilon_t S_{ji} - \tfrac{2}{3}\delta_{ji}\rho k$$

$$S_{ji} = \frac{1}{2}\left[\frac{\partial u_j}{\partial x_i} + \frac{\partial u_i}{\partial x_j}\right] - \frac{1}{3}\delta_{ji}\frac{\partial u_k}{\partial x_k}$$

For the purpose of this paper, we will define RANS turbulent viscosity as

$$\upsilon_t^{\text{RANS}} = f_\mu C_\mu \frac{k^2}{\varepsilon} \tag{4}$$

A. Hybrid RANS/LES

Nichols and Nelson [2] give an example of a hybrid RANS/LES turbulence model. This method was implemented in conjunction with Menter's shear stress transport two-equation turbulence model and is termed a *multiscale model*. In the present paper, the hybrid model is used with the two-equation model described in Eqs. (2) and (3). The turbulent length scale used in this implementation is defined as

$$l_t = \max(6.0\sqrt{\upsilon_t^{\text{RANS}}/\Omega}, k^{3/2}/\varepsilon) \tag{5}$$

The subgrid turbulent kinetic energy is defined as

$$k^{\text{LES}} = f_d k \tag{6}$$

The damping function is defined as

$$f_d = \{1.0 + \tanh[2\pi(\Lambda - 0.5)]\}/2 \tag{7}$$

where

$$\Lambda = \frac{1}{1 + [l_t/\Delta]^{4/3}} = \frac{1}{1 + \lambda^{4/3}} \tag{8}$$

λ is the unresolved characteristic ratio, and

$$\Delta = \max(\Delta_x, \Delta_y, \Delta_z) \tag{9}$$

The eddy viscosity is then calculated from

$$\upsilon_t = f_d \upsilon_t^{\text{RANS}} + (1.0 - f_d)\upsilon_t^{\text{LES}} \tag{10}$$

$$\upsilon_t^{\text{LES}} = \min(\upsilon_t^{\text{RANS}}, 0.084\Delta\sqrt{k^{\text{LES}}}) \tag{11}$$

Note that this hybrid model allows the transition from RANS to LES as a function of local grid spacing and local turbulent length scale predicted by the RANS model rather than as a function of the grid spacing alone. This allows the model to detect whether it can resolve the turbulent scales present on the existing grid before its transition over to the LES mode.

B. PANS Approach

In its original form, PANS [5] replaces the two-equation turbulence model by solving for the unresolved kinetic energy k_u and the dissipation ε_u. The k_u equation is identical to the original k equation. The dissipation equation has only one major change through

$$\tilde{C}_{\varepsilon 2} = f_k(C_{\varepsilon 2} - C_{\varepsilon 1}) + C_{\varepsilon 1} \tag{12}$$

In the present work, we introduce an attempt to use a variable f_k instead of a constant value. We use Eq. (7) to compute f_k as

$$f_k = \{1.0 + \tanh[2\pi(\Lambda - 0.5)]\}/2 \tag{13}$$

In this case, the turbulent length scale is defined as

$$l_u = \frac{k_u^{3/2}}{\varepsilon_u}, \qquad \Lambda = \frac{1}{1+\lambda^{4/3}}, \qquad \text{and} \quad \lambda = \frac{l_u}{\Delta}$$

The function in Eq. (13) has the characteristic to be equal to 1.0 in the viscous sublayer, as the unresolved characteristic ratio tends to be of very small value. Also, the value of this function is restricted to 1, in case the RANS turbulent viscosity becomes smaller than the LES viscosity (11).

C. Boundary Conditions

In the present study, a characteristic Riemann invariant-type boundary condition was used to model the far-field boundaries, while a periodic boundary condition was imposed in the longitudinal direction of the cylinder. A no-slip velocity boundary condition was used at the cylinder surface so that the fluid would neither slip nor penetrate. For the case of the stationary cylinder, there is no relative motion between the cylinder surface and the fluid, and the velocity components were set to zero. For the rotating cylinder, the velocity at the cylinder surface was set to be equal to $\bar{\omega} \times \bar{r}$, where $\bar{\omega}$ is the cylinder angular velocity and $\bar{r}$ is the position vector connecting the cylinder axis of rotation to the cylinder surface, as shown in Fig. 1a. The interface to the new rotating/spinning boundary condition resides in the `user.cont` file. The user has to specify the angular velocity (rad/s), the axis of rotation, and a point on the axis. Vector $\bar{r}$ is the vector with the minimum distance between the rotating surfaces to the axis of rotation and is defined as

$$d = \frac{|(x_2 - x_1) \times (x_1 - x_0)|}{|x_2 - x_1|}$$

where x_1 and x_2 are points on the axis of rotation while x_0 is a point on the surface of the cylinder.

III. Results and Discussion

Flow past a stationary cylinder as well as a rotating circular cylinder was computed to verify the time accuracy of the code and of the relative advantage of the hybrid turbulence models RANS/LES and PANS. The two-dimensional grid consisted of 32,256 cells and 24 blocks, and extended 15 diameters into the far field (Fig. 1b). The three-dimensional grid was the same as the two-dimensional grid with the addition of 40 planes, which covered the two-cylinder diameter. This grid is the best grid tested by Travin et al. [14] and was also used by Vatsa and Singer [15] in their studies of the cylinder case. The same grid was used for all runs, which gave a first grid y^+ range of approximately 0.2–2.0. The diameter D of the cylinder was 40 mm wide at $Re = 50,000$ and the Mach number for all cylinder cases was set at a value of $M = 0.3$. A nondimensional time step of 0.015 (based on freestream speed and the diameter of the cylinder) was used for all cases. Based on the Strouhal number range and the time step used for the present cases, approximately 350 data points in time per cycle of shedding was sampled. Four subiterations were used to reduce the error. Each of the 2-D simulations required approximately 3 h using 24 (2.8 GHz P-4) computers. The 3-D cases each required approximately 48 h using the same set of 24 computers.

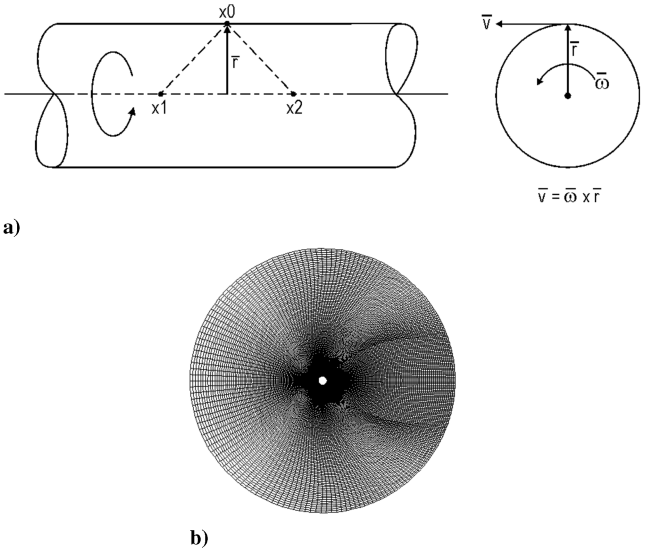

Fig. 1 Images of a) rotation boundary condition and b) grid distribution for a circular cylinder [11].

A. Stationary Circular Cylinder in Crossflow

The shedding frequencies are determined from the lift coefficient C_L fluctuation as it varies with time (Fig. 2). The C_L is obtained via the internal force and moment integration algorithm, Post [16]. The strategy for this case was to first run the simulation at a very coarse grid level (1/4th in each direction) for 10,000 iterations, to trigger its asymmetric vortex shedding instability, and then refine the grid and run the solution for an additional 20,000 iterations. The solutions were averaged over the last 15,000 iterations (approximately 50 shedding cycles). The onset of asymmetric vortex shedding is seen to occur just after the first 60 time units, and the switch to fine grid is seen to coincide with an increase in amplitude. It was observed that approximately four subiterations per physical time step produced the optimal convergence per iteration. However, the physics of the specific problem will dictate the subiteration number for other cases. In the present results, four subiterations typically reduced the residual by three orders of magnitude at that time level, with no improvement using more iteration. The results were compared with the results using up to 20 subiterations, with no substantial difference in the final results.

The Strouhal number St was captured with the use of the power spectral density (PSD) of C_L as shown in Fig. 3. To verify the capability of PAB3D for simulating unsteady flow problems, the turbulent separated (TS) case was used, which simulates the experimental flow condition in which the boundary layer is tripped well ahead of separation. Similar to what was found by other researchers [14,15,17], we achieved this objective numerically by choosing a freestream turbulence level high enough to cause natural transition (5 times laminar viscosity). We performed 2-D RANS computations with PAB3D using two-equation $k\varepsilon$ at the Reynolds number of 140,000. This flow condition matched the conditions used by Travin et al. [14], Vatsa and Singer [15] and Hansen and Forsythe [17]. The results from the work by Travin et al. [14] show that there are only small differences observed between the 2-D RANS, 3-D RANS, and 3-D DES results. For this reason, we will not present any 3-D results for this case. The time-averaged surface pressure

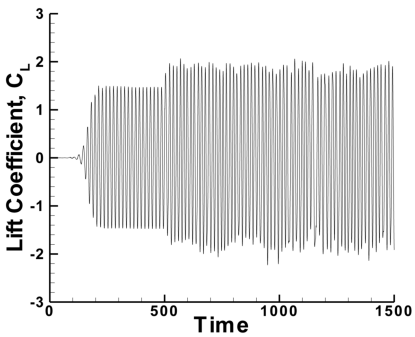

Fig. 2 Lift coefficient C_L fluctuations with time using the 2-D PANS formulation.

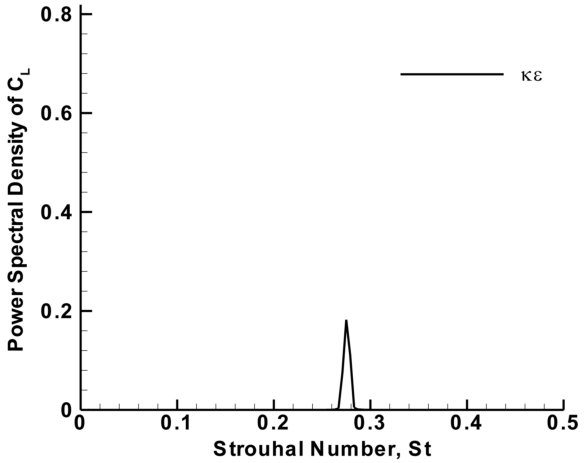

Fig. 3 Power spectral density vs Strouhal number using $k\varepsilon$ RANS formulation for $Re = 140,000$.

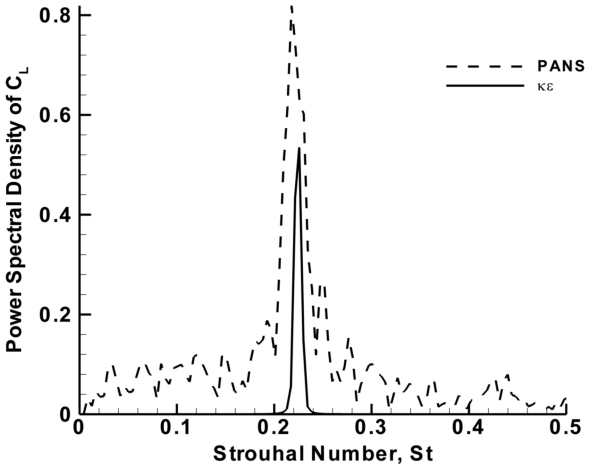

Fig. 5 Power spectrum density vs Strouhal number results from PANS and $k\varepsilon$ RANS formulations (LS case).

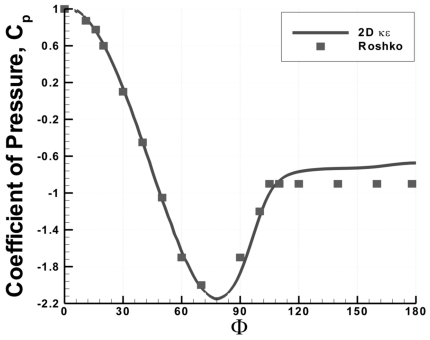

Fig. 4 Comparison between coefficient of pressure on the cylinder surface using 2-D $k\varepsilon$ RANS and experimental data of Roshko's [10] (TS case).

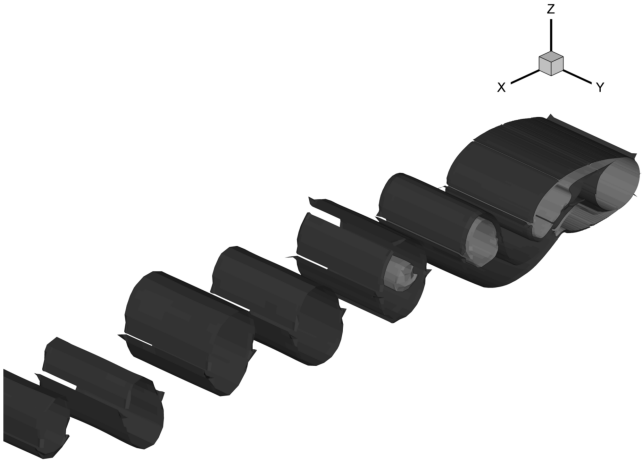

Fig. 6 Three-dimensional vorticity magnitude results from RANS simulation (LS case).

coefficients C_P resulting from the 2-D computations were compared with the experimental data of Roshko [10] in Fig. 4. Table 1 compares the present PAB3D results using the 2-D $k\varepsilon$ turbulence model with the 3-D DES studies done by Travin et al. [14] and Hansen and Forsythe [17] and the experiment of Roshko [10]. Based on the results listed in Table 1 and the comparisons of Fig. 4, it was concluded that the current RANS compared well with Roshko's experimental data and with other CFD simulations.

The laminar separated (LS) case was chosen to evaluate the implementations of both hybrid RANS/LES and PANS formulations into the PAB3D code and to investigate their capability to simulate such flow. This case is compared with the experimental data of Nordberg [18] ($Re = 3000$ and 8000) and Cantwell and Coles [19] ($Re = 140,000$). Figure 5 shows the PSD variation with the Strouhal number from RANS and PANS results. It is clear that RANS produced a peak at only one major Strouhal number and no significant spectral energy at higher Strouhal numbers. This result indicates that the 3-D RANS simulation has a two-dimensional flow character. The vorticity plot shown in Fig. 6 supports this conclusion, as it shows the flow with no change in the Y direction. On the other hand, the PANS resulted in one major Strouhal number and several minor ones, indicating that more scales were resolved in this simulation. Similar observations were made for the RANS/LES simulation. Figure 7 shows the three-dimensional character of the flow produced as a result of the PANS formulation. Table 2 shows the comparison between the recent PAB3D simulations, Travin et al. [14] DES solutions, and the experimental data. The PANS formulation in PAB3D produces the closest results compared with the experimental data. The 2-D PANS and LES results largely differ from

Table 1 $Re = 140,000$ TS time-averaged results

Method	C_D	C_{pb}	St
3-D DES Travin et al. [14]	0.57	0.65	0.3
Hansen and Forsythe [17]	0.59	0.72	0.29
PAB3D $k\varepsilon$	0.62	0.68	0.27
Experiment	0.62–0.74	0.5–0.9	0.27

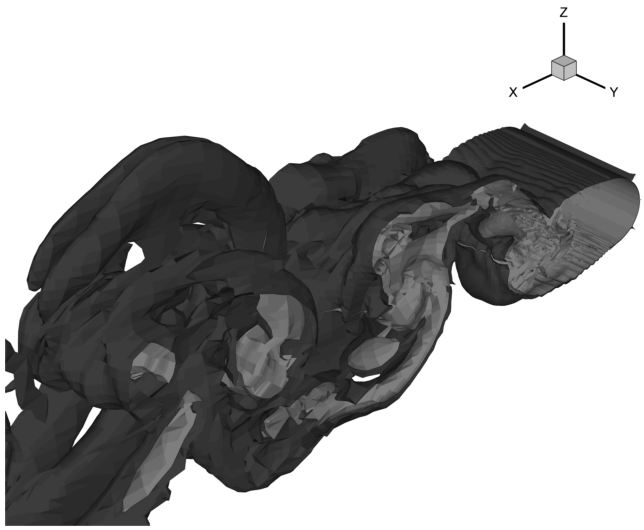

Fig. 7 Three-dimensional vorticity magnitude results from PANS formulation (LS case).

Table 2 $Re = 50,000$ TS time-averaged results

Method	C_D	$-C_{pb}$	St
3-D DES Travin et al. [14]	1.27	1.28	0.21
2-D DES Travin et al. [14]	1.77	2.05	0.14/0.20
2-D PAB3D RANS/LES	1.69	2.05	0.21
2-D PAB3D PANS	1.67	2.1	0.22
3-D PAB3D RANS/LES	1.0	0.9	0.22
3-D PAB3D PANS	1.1	1.03	0.21
2-D/3-D PAB3D RANS	1.08	1.03	0.23
Experiment	0.98–1.25	0.9–1.2	0.18–0.21

the experimental data, but are similar in character to the 2-D DES simulations of Travin et al. [14].

Figure 8 shows the variations of C_L with respect to time for the PANS formulation. The 3-D PANS solution displayed large and random variations, as a result of strong modulation of the vortex shedding. These observations are similar to the ones reported by Travin et al. [14] and Vatsa and Singer [15], using 3-D DES

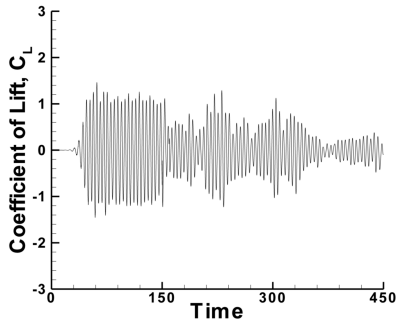

Fig. 8 Lift coefficient C_L fluctuations with time results from 3-D PANS formulation (LS case).

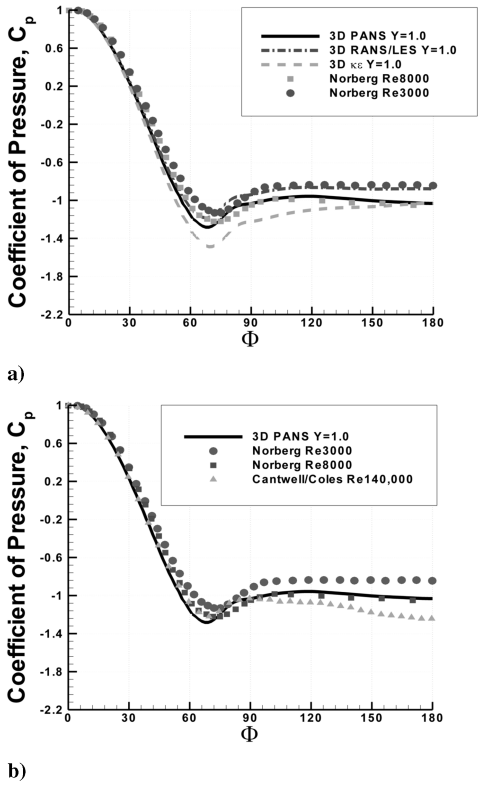

Fig. 9 Coefficient of pressure on the cylinder surface results from a) 3-D $k\varepsilon$ RANS, RANS/LES, and PANS formulation at $Y = 1.0$ (LS case) and b) 3-D PANS formulation compared with experimental data (LS case).

formulation. The time-averaged surface pressure distributions from the 3-D simulations are compared with experimental data of Nordberg [18] and Cantwell and Coles [19] in Fig. 9. In general, the hybrid RANS/LES and PANS formulations produced comparable results to the 3-D DES solutions presented in [14,15].

Figure 10 shows the unresolved turbulent kinetic energy resulting from the RANS and PANS formulations. The levels from the RANS simulation were 10 times those produced by the PANS formulation. More energy was resolved using the PANS formulation as compared with that produced by the RANS simulations. Figure 11 shows the time-averaged f_k from the PANS simulations. The f_k was as low as 0.3 in the region of interest, where more energy was resolved through the use of the PANS formulation. The smaller the f_k value, the more LES-like simulations are produced. The closer f_k is to a value of 1, the more RANS-like are the simulation results. This occurs in the viscous sublayer and far-field regions, as expected, where the grid resolution is enough for the use of RANS.

B. Rotating Circular Cylinder in Crossflow

The computational grid described earlier and shown in Fig. 1b was used to compute the flowfield around a rotating cylinder. The flowfield has been computed both in 2-D and 3-D modes using the standard $k\varepsilon$ turbulence model and the hybrid turbulence models

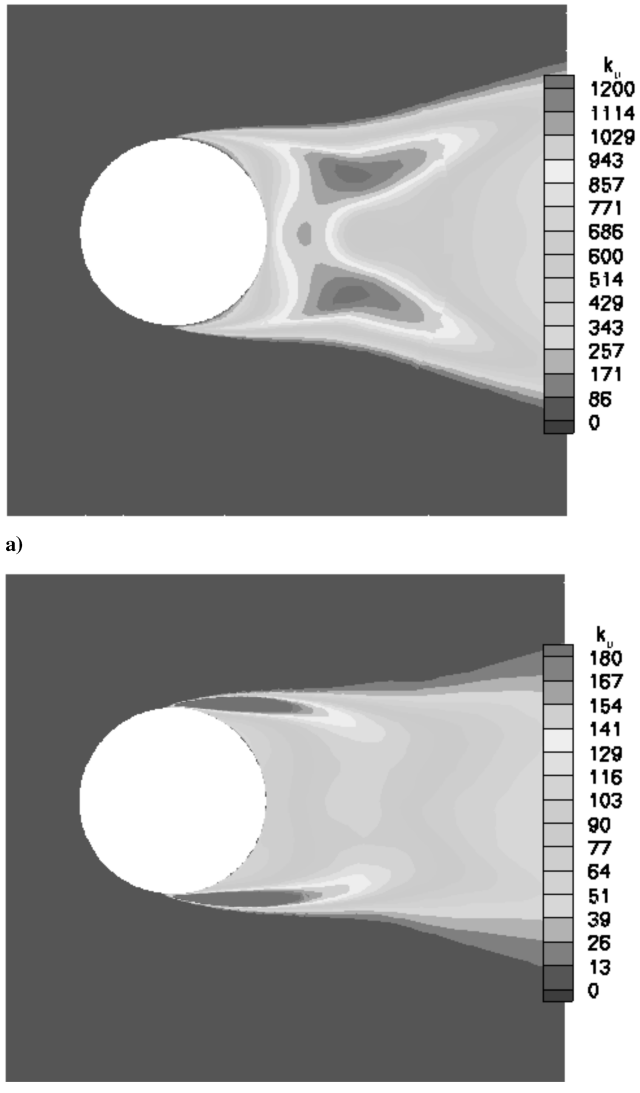

Fig. 10 Unresolved turbulent kinetic energy k_u (m^2/s^2) contours at $Y = 1.0$ produced from a) RANS simulation (LS case) and b) PANS simulation (LS case).

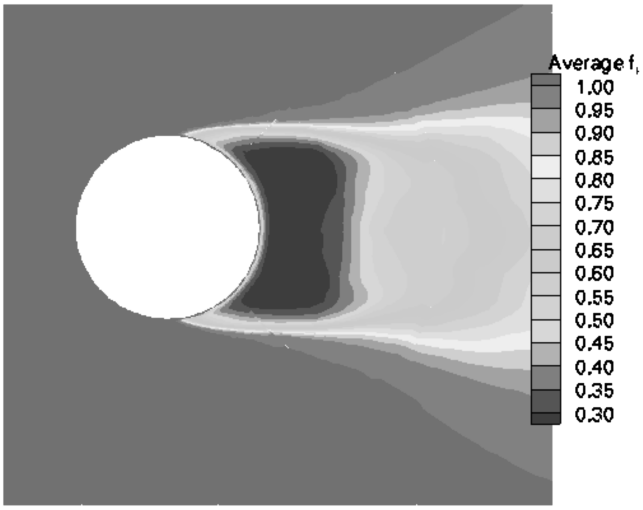

Fig. 11 Averaged f_k contours at $Y = 1.0$ from PANS simulation (LS case).

RANS/LES and PANS. Three main parameters govern the flow around rotating cylinders: the Reynolds number, the ratio of peripheral to freestream velocity, and the cylinder aspect ratio.

In the present calculation, the rotational speed of the cylinder varied from 0 to 10,000 rpm; the freestream Mach number was 0.3 and the $Re = 50,000$. The same solution strategy used to compute the flowfield around the stationary cylinder was used for the rotating cylinder cases. The variation in the time-averaged C_L with respect

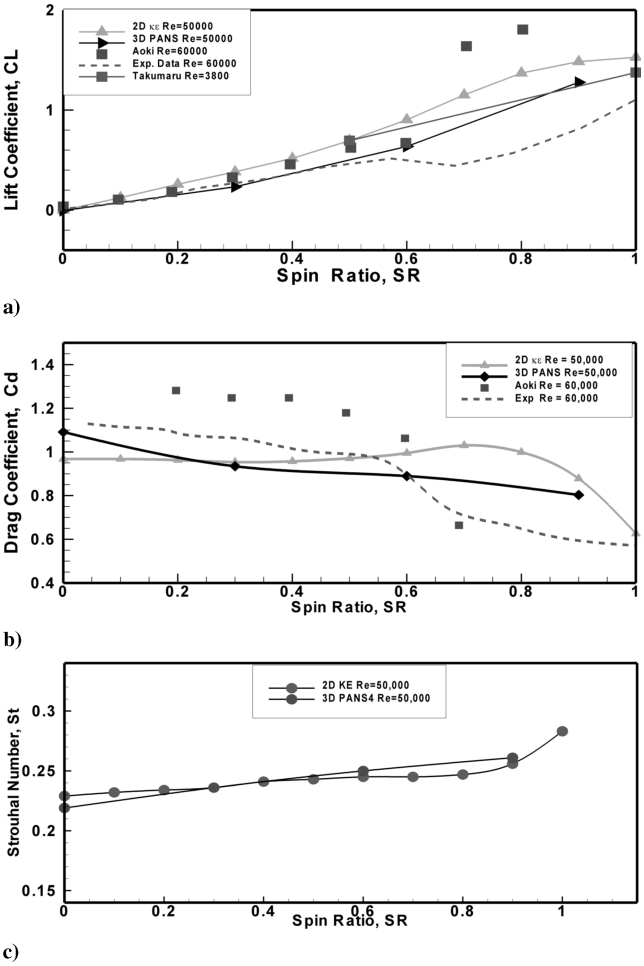

Fig. 12 Plots of a) lift coefficient for various spin ratios, b) drag coefficient for various spin ratios, and c) computed Strouhal number.

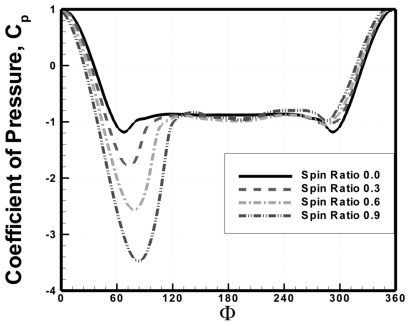

Fig. 13 Effect of spin ratio on the coefficient of pressure.

to the spin ratio (SR) is shown in Fig. 12a. SR is defined as the ratio between the peripheral velocity u of the cylinder to the freestream velocity U. The rotation of the cylinder generated lift and C_L increased with increasing SR. Comparison between the present calculations and the results of Aoki et al. [12] and Tokumaru et al. [13] showed good agreement. Simulations using 3-D hybrid RANS/PANS yielded results that are closer to the experimental data [12]. Variation of the C_D with respect to the SR is shown in Fig. 12b. For the range of speeds computed in the present study, the coefficient of drag tends to decrease with increasing SR. The Strouhal number for the rotating cylinder was captured using the PSD of C_L as explained earlier. The range of the Strouhal number for the rotating cylinder varied between the values of 0.23 and 0.28. The variation of the Strouhal number with SR is shown in Fig. 12c. Increasing the SR tends to increase the Strouhal number; however, there was no significant change in the Strouhal number between the 2-D and 3-D calculations.

Figure 13 shows the time-averaged surface pressure distribution as a result of the 3-D PANS simulation for the SR of 0.0, 0.3, 0.6, and 0.9, respectively. For the stationary cylinder (SR = 0.0), C_p distribution is symmetrical around the cylinder. As the SR increased, the pressure distribution became asymmetric due to the spinning, and the fact that the net turning of the flow produced lift. Corresponding pressure contours are shown in Fig. 14. The freestream flow over the top of the cylinder follows the induced flow from the spinning, while the freestream below the cylinder is opposed by the induced flow. This results in an accelerated flow on the top half of the cylinder.

IV. Conclusions

A hybrid turbulence model RANS/LES and PANS have been added to the PAB3D code. The new capabilities improve the accuracy of simulating an unsteady flowfield. In this paper, a new approach to prescribe the unresolved kinetic energy parameter f_k function was proposed. The parameter f_k is a function of length scale and grid size, which represents a characteristic length scale. Some of the drawbacks of such a function are that it varies with time and space, and that it could be affected by grid resolution. The PANS approach is much simpler to implement in most CFD codes than other approaches such as DES and RANS/LES. The preliminary results provide a preview of the potential capability of PANS in simulating unsteady and complex flow phenomena. The PAB3D code using 3-D PANS captured both temporal and spatial fluctuations, and solutions compared well with the experimental data.

The TS and LS flows were simulated for a stationary cylinder. The TS case was accurately simulated using a general two-equation $k\varepsilon$ turbulence model (eddy-viscosity model) without any enhancement. PAB3D accurately predicted the drag coefficient C_D and the Strouhal number. The LS case posted a great challenge for the eddy-viscosity turbulence models. The RANS/LES and the PANS approaches in the CFD code provided much better predictions when compared to measured data. We have observed much better predictions of C_D, the Strouhal number, and the surface pressure distribution than the results with the $k\varepsilon$ turbulence model.

In the case of a rotating cylinder, the present calculations indicate that with an increase of the rotational speed, C_L increases while C_D

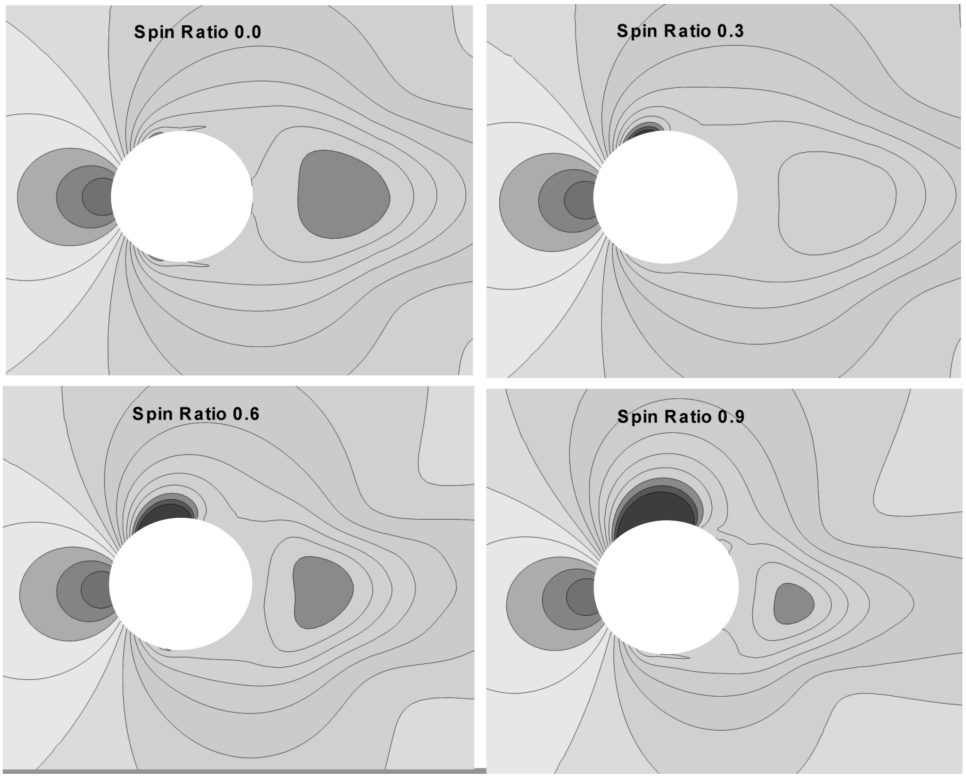

Fig. 14 Averaged pressure contours for 3-D PANS for SR = 0.0, 0.3, 0.6, and 0.9.

decreases. The PANS provided the best comparison with the experimental data. The computed Strouhal number is in the range of 0.22–0.28, which is in good agreement with previously published results.

Future work will involve explorations of a new approach to improve the accuracy and robustness of creating a simulation of an unsteady flowfield. This can be accomplished through the implementation of a novel two-stage procedure to efficiently estimate the level of scale resolution possible for a given flow on a given grid for PANS and other hybrid models.

Acknowledgments

A. Elmiligui and S. J. Massey would like to acknowledge the support of NASA Langley Research Center for providing the funding needed to carry out this work. The authors wish to thank Veer Vatsa of NASA Langley Research Center for providing the grid and many helpful discussions. Furthermore, the authors are thankful to Robert Hansen of the United States Military Academy for providing some of the data presented in this work.

References

[1] Spalart, P. R., "Young Person's Guide to Detached Eddy Simulation Grids," NASA CR-2001, 211032, 2001.

[2] Nichols, R. H., and Nelson, C. C., "Application of Hybrid RANS/LES Turbulence Models," AIAA Paper 2003-0083, 2003.

[3] Mani, M., and Paynter, C. C., "Hybrid Turbulence Models for Unsteady Simulation of Jet Flows," AIAA Paper 2002-2959, 2002.

[4] Batten, P., Goldberg, U., and Chakravarthy, S., "LNS—An Approach Towards Embedded LES," AIAA Paper 2002-0427, 2002.

[5] Girimaji, S. S., Sreenivasan, R., and Jeong, E., "PANS Turbulence Model For Seamless Transition Between RANS, LES: Fixed-Point Analysis and Preliminary Results," 4th ASME-JSME Joint Fluids Engineering Conference, American Society of Mechanical Engineers, Fluids Engineering Div., Paper FEDSM2003-45336, 13–16 July 2003.

[6] Abdol-Hamid, K., and Girimaji, S., "A Two-Stage Procedure Toward the Efficient Implementation of PANS and Other Hybrid Turbulence Models" NASA TM-213260, 2k004

[7] *PAB3D Code Manual*, Propulsion Aerodynamics Branch, NASA Langley Research Center and Analytical Services and Materials, Inc., Hampton, VA, http://www.asm-usa.com/PAB3D/

[8] Massey, S. J., and Abdol-Hamid, K. S., "Enhancement and Validation of PAB3D for Unsteady Aerodynamics," AIAA Paper 2003-1235, 2003.

[9] Morkovin, M., "Flow Around a Circular Cylinder—A Kaleidoscope of Challenging Fluid Phenomena," *Proceedings of ASME Symposium on Fully Separated Flows*, American Society of Mechanical Engineers, Fairfield, NJ, 1964, pp. 102–118.

[10] Roshko, A., "Experimental on Flow Past a Circular Cylinder at Very High Reynolds Number," *Journal of Fluid Mechanics*, Vol. 10, No. 3, 1961, pp. 345–356.
DOI: 10.1017/S0022112061000950

[11] Schlichting, H., *Boundary-Layer Theory*, McGraw–Hill, New York, 1979.

[12] Aoki, K., Ito, T., and Nakayama, Y., "Flow Characteristics Around a Rotating Cylinder," *Proceedings of the School of Engineering of Tokai University*, Vol. 26, pp. 29–34, 2001.

[13] Tokumaru, P. T., and Dimotakis, P. E., "The Lift of a Cylinder Executing Rotary Motions in a Uniform Flow," *Journal of Fluid Mechanics*, Vol. 255, Feb. 1993, pp. 1–10.
DOI: 10.1017/S0022112093002368

[14] Travin, A., Shur, M. L., Strelets, M., and Spalart, P. R., "Detached-Eddy Simulation Past a Circular Cylinder," *Flow, Turbulence and Combustion*, Vol. 63, Nos. 1–4, Jan. 2000, pp. 193–313.
DOI: 10.1023/A:1009901401183

[15] Vatsa, V. N., and Singer, B. A., "A Comparison of Evaluating a Second-Order Accurate Navier-Stokes Code for Detached Eddy Simulation Past a Circular Cylinder," AIAA Paper 2003-4085, 2003.

[16] Massey, S. J., *POST Code Manual*, http://eagle.com/post/ [retrieved 2003].

[17] Hansen, R. P., and Forsythe, J. R., "Large and Detached Eddy Simulations of a Circular Cylinder Using Unstructured Grids," AIAA Paper 2003-0775, 2003.

[18] Nordberg, C., "Effects of Reynolds Number and Low Intensity Free-Stream Turbulence on Flow Around a Circular Cylinder," Publ. 87/2, Dept. of Applied Thermosciences and Fluid Mechanics, Chalmers Univ. of Technology, Gothenburg, Sweden, 1987.

[19] Cantwell, B., and Coles, D., "An Experimental Study of Entrainment in the Turbulent Near Wake of a Circular Cylinder," *Journal of Fluid Mechanics*, Vol. 136, Nov. 1983, pp. 321–374.
DOI: 10.1017/S0022112083002189